From entropy to compression: Competing thermodynamic drivers of structural transitions in transition metals

S. Azadi [1,2,3,*] S. M. Vinko [2] A. Principi [1] T. D. Kühne [3,4,5] and M. S. Bahramy [1]

[1]*Department of Physics and Astronomy, University of Manchester, Oxford Road, Manchester M13 9PL, United Kingdom*
[2]*Department of Physics, Clarendon Laboratory, University of Oxford, Parks Road, Oxford OX1 3PU, United Kingdom*
[3]*Center for Advanced Systems Understanding, Untermarkt 20, D-02826 Görlitz, Germany*
[4]*Helmholtz Zentrum Dresden-Rossendorf, Bautzner Landstraße 400, D-01328 Dresden, Germany*
[5]*Chair of Computational System Sciences, Institute of Artificial Intelligence, TU Dresden, Nöthnitzer Straße 46, D-01187 Dresden, Germany*

(Received 18 May 2026; accepted 29 September 2026; published 12 November 2026)

Structural phase transitions in metals are conventionally described in terms of external pressure and density, while electronic entropy is typically regarded as a secondary correction to the free energy. Here, we show that electronic entropy constitutes a thermodynamic control parameter of comparable importance to external pressure in determining structural stability. Using finite-temperature density functional theory, we construct pressure–electronic-temperature phase diagrams for 15 transition metals spanning the hcp, fcc, and bcc families and systematically investigate the competition between compressive and entropic contributions to the free energy. We find that increasing electronic entropy progressively reshapes the free-energy landscape, reducing structural competition and driving universal trends in phase stability across chemically diverse metals. In contrast, external pressure often acts in opposition, stabilizing structures that are suppressed by electronic excitation. The resulting phase behavior cannot be understood from pressure alone but emerges from the balance between these two thermodynamic driving forces. Our results establish a general framework for understanding structural transformations in electronically excited matter, extend the conventional pressure-temperature description of metals by explicitly incorporating electronic entropy, and provide quantitative predictions for ultrafast laser and x-ray free-electron laser experiments operating far from equilibrium.

DOI: 10.1103/918j-rz63

I. INTRODUCTION

The structural and thermodynamic properties of metals are conventionally described in terms of external variables such as pressure, density, and lattice temperature [1–5]. Under strong electronic excitation, however, this picture breaks down as the electronic subsystem can be driven far from equilibrium and transiently decoupled from the lattice. In this regime, electrons occupy a broad range of energy states, leading to significant modifications of bonding, screening, and interatomic forces. These changes can induce structural transformations on ultrafast timescales, providing access to states of matter that lie outside conventional equilibrium phase diagrams. Transition metals, with their partially filled *d* bands and pronounced structure in the electronic density of states near the Fermi level, are particularly sensitive to such electronic perturbations and therefore offer an ideal platform to explore these effects.

To investigate this regime systematically, we perform a finite-temperature density functional theory (FT-DFT) study of 15 metals spanning hcp-, fcc-, and bcc-ground-state structures. By constructing Gibbs free-energy phase diagrams over a wide pressure-temperature range, we identify clear trends in how structural stability evolves under electronic excitation. Increasing electronic temperature reduces the diversity of stable phases and drives a redistribution of stability toward simpler crystal structures. In particular, the fcc phase becomes increasingly prevalent at elevated temperatures, while the hcp phase persists as a secondary competitor and bcc stability is progressively confined to higher-pressure conditions. Despite these global trends, the detailed phase behavior remains strongly material dependent, reflecting differences in electronic structure and atomic volume across the periodic table.

This behavior can be understood in terms of the competing roles of electronic excitation and mechanical compression. Electronic excitation modifies the distribution of electrons over available states, alters screening, and changes the effective interatomic interactions, favoring more isotropic metallic bonding and stabilizing close-packed structures. In contrast, compression favors structures with smaller atomic volumes, most notably the bcc phase. Structural stability therefore emerges from a balance between these effects, with temperature and pressure selecting among a reduced set of competing crystal structures. This interplay provides a unified

*Contact author: sam.azadi@manchester.ac.uk

Published by the American Physical Society under the terms of the Creative Commons Attribution 4.0 International license. Further distribution of this work must maintain attribution to the author(s) and the published article's title, journal citation, and DOI.

interpretation of the trends observed across the calculated phase diagrams.

Experimentally, such conditions can be realized using ultrafast pump-probe techniques, including femtosecond optical lasers and x-ray free-electron lasers (XFELs), which rapidly increase the electronic temperature while leaving the ionic subsystem comparatively cold [6–21]. On femtosecond timescales, electron-electron scattering establishes a hot electronic distribution, whereas energy transfer to the lattice occurs more slowly. This separation allows materials to transiently explore high-temperature electronic states at nearly fixed atomic positions, such that structural stability is governed by the electronic free energy. The resulting transformations constitute nonthermal, electronically driven solid-solid phase transitions [22–26], commonly described within the framework of the two-temperature model [27,28].

The theoretical description employed here is based on Mermin's finite-temperature extension of density functional theory [29–33], which provides a self-consistent framework for treating temperature-dependent occupations, screening, and exchange-correlation (XC) effects. Within this approach, the electronic free energy is obtained directly, enabling a quantitative description of phase stability under electronic excitation. The results presented here establish electronic excitation as a key factor in controlling structural stability in metals and provide a coherent framework for interpreting phase transitions under nonequilibrium conditions. By linking electronic effects with pressure-driven stabilization, this work offers guidance for ultrafast experiments and suggests routes for controlling material properties through electronic excitation.

II. COMPUTATIONAL DETAILS AND METHODS

A. Theoretical background

Electronic entropy is treated within a finite-temperature formalism through the Fermi-Dirac occupation of electronic states, yielding the entropy contribution to the Gibbs free energy $G = E - TS + PV$, where E, T, P, and V are ground-state electronic energy, temperature, external volumetric pressure, and volume of the system, respectively. The entropy S can be written as

$$S(T) = -k_B \int n(E)[f(E)\ln f(E) + (1 - f(E))\ln(1 - f(E))]dE, \quad (1)$$

where k_B, $n(E)$, and $f(E)$ are the Boltzmann constant, the electronic density of states, and the Fermi-Dirac distribution function, respectively. The electronic entropy depends on the temperature through the Fermi-Dirac distribution, which in general form is given by

$$f(E,T) = \left[1 + \exp\left[\left(E - \frac{\mu}{k_B T}\right)\right]\right]^{-1}, \quad (2)$$

with μ and E as the chemical potential and ground-state electronic energy, respectively. For most metals at low and near-room temperatures, the electronic entropy is well described within the Sommerfeld expansion [34], $S = \gamma T$, where the Sommerfeld coefficient γ is proportional to the electronic density of states at the Fermi level, $n(E_F)$. In this regime, the entropy contribution is small and varies linearly with temperature, so its influence on structural, elastic, and thermodynamic properties is typically negligible [35,36].

At elevated electronic temperatures, the entropy term $-TS$ becomes a dominant contribution to the free energy, enabling entropy-driven changes in phase stability. A consistent theoretical description of these effects requires an explicit finite-temperature electronic free-energy formalism, such as FT-DFT. The Kohn-Sham (KS) equation at electronic temperature T, which is solved self-consistently, is given by

$$\left(\frac{-\nabla^2}{2} + V^T(\mathbf{r})\right)\phi_i^T(\mathbf{r}) = \varepsilon_i^T \phi_i^T(\mathbf{r}), \quad (3)$$

where the first term is the kinetic energy, ε_i^T and $\phi_i^T(\mathbf{r})$ are KS eigenvalue and eigenfunction, respectively, and

$$V^T(\mathbf{r}) = V_{\text{ext}}(\mathbf{r}) + V_H^T(\mathbf{r}) + V_{\text{xc}}^T(\mathbf{r}), \quad (4)$$

where V_{ext}, V_H, and V_{xc} are external, Hartree, and exchange-correlation potentials, respectively. The density is given by

$$n(\mathbf{r},T) = \sum_i f_i^T \left|\phi_i^T(\mathbf{r})\right|, \quad (5)$$

with

$$f_i^T = \left[1 + \exp\left(\frac{\varepsilon_i^T - \mu}{T}\right)\right]^{-1}, \quad (6)$$

where μ is the chemical potential. It should be noted that, although f_i^T is similar to the Fermi-Dirac function for non-interacting electrons, the difference is that for KS electrons, f_i^T depends also implicitly on T through the KS eigenvalues ε_i^T.

FT-DFT has proven to be a powerful practical framework for investigating materials under conditions of thermal electronic excitation, most commonly within the generalized-gradient approximation for the XC functional [30]. Although the conventional local-density approximation (LDA) becomes less accurate in regimes of high electronic temperature and density, recent developments may improve the accuracy of LDA for large electronic densities and finite temperatures [37–41].

B. Phase-diagram calculations

To construct pressure-temperature (P-T) phase diagrams, we performed systematic FT-DFT calculations for each crystal structure on a dense two-dimensional (P,T) grid. For each element and each structure (hcp, fcc, and bcc), the Gibbs free energy was evaluated over the range 0 GPa $< P <$ 300 GPa, 0.1 eV $< T <$ 4.1 eV, using pressure increments of 20 GPa and temperature increments of 0.1 eV, resulting in 496 grid points per structure. At each grid point, calculations were carried out at fixed volume corresponding to the target pressure, and the electronic free energy was obtained self-consistently. At each external pressure (corresponding to the horizontal axis of the P-T phase diagrams), the crystal structures and lattice parameters, including the c/a ratio for hcp phases, were first optimized at a low electronic temperature of 0.002 eV while the symmetry of system was

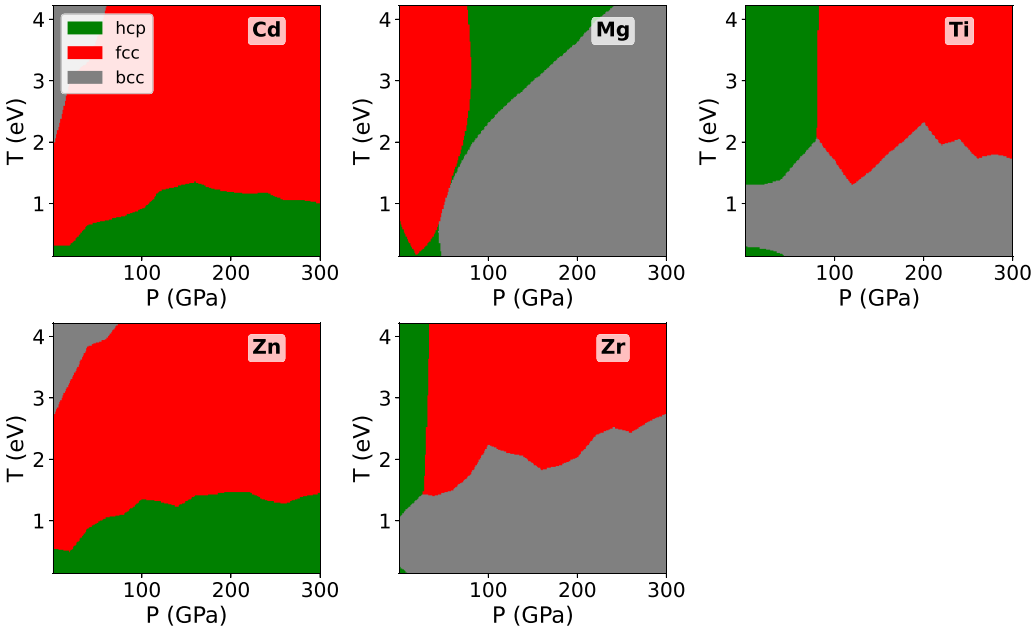


FIG. 1. Gibbs free-energy phase diagrams of hcp-ground-state transition metals (Cd, Mg, Ti, Zn, and Zr) as a function of pressure and electronic temperature. At each (P, T) point, the stable phase is determined from the minimum Gibbs free energy among hcp, fcc, and bcc structures. The equilibrium atomic volume of the stable phase at each point is shown separately in Fig. 3, with representative values at the pressure extremes collected in Table I. The diagrams reveal a wide range of structural responses under electronic excitation. Cd and Zn exhibit a crossover from hcp at low temperature to fcc over most of the phase space, with only limited bcc stability. In contrast, Mg is largely dominated by the bcc phase, reflecting strong stabilization by compression. Ti displays pronounced three-phase competition, with hcp favored at low pressure, bcc stabilized at higher pressure, and fcc emerging at elevated temperatures. Zr shows a strong pressure-dependent competition between bcc and fcc, while hcp remains stable only near low-pressure conditions.

conserved. The stable phase at each (P, T) point was determined by direct comparison of the free energies of the competing structures. To obtain smooth phase boundaries and improve visualization of the phase diagrams, the discrete free-energy data were interpolated using a regular grid interpolation scheme. This procedure provides a continuous representation of the free-energy landscape while preserving the underlying first-principles data. Phase boundaries were extracted from the interpolated free-energy differences between competing phases. The phase diagrams were constructed from ∼7500 FT-DFT calculations on a dense P-T grid, ensuring a systematic and high-resolution mapping of structural stability.

C. Electronic structure calculations

All electronic structure calculations were performed using the QUANTUM ESPRESSO package (version 7.4) [42]. The Perdew-Burke-Ernzerhof generalized-gradient approximation was employed for the exchange-correlation functional [43]. projector augmented wave (PAW) pseudopotentials were used, with a plane-wave kinetic-energy cutoff of 150 Ry and an augmentation-charge cutoff of 1500 Ry. Electronic occupations were treated using the Fermi-Dirac distribution at temperature T. The number of empty bands was increased systematically with temperature to ensure convergence of both the internal energy and entropy contributions. Brillouin-zone integrations were performed using Monkhorst-Pack k-point meshes $24 \times 24 \times 24$, chosen to ensure convergence of total energies within a few meV per atom. Convergence tests with respect to k-point sampling, plane-wave cutoff, and number of empty bands were performed to ensure that free-energy differences between competing phases are converged within a few meV per atom.

III. RESULTS AND DISCUSSION

A. Gibbs free-energy phase diagram

The Gibbs free-energy phase diagrams of the hcp-ground-state metals display the richest diversity among the three structural classes. Cd and Zn are largely governed by competition between hcp and fcc phases, with bcc appearing only in limited regions, indicating that increasing electronic temperature primarily stabilizes fcc in these systems. In contrast, Mg is predominantly bcc over much of the pressure-temperature range, demonstrating strong volume-driven stabilization of the bcc phase. Ti exhibits full three-phase competition, with hcp favored at low pressure and temperature, bcc stabilized by compression, and fcc emerging at higher temperatures. Zr shows a similarly strong competition between bcc and fcc, while hcp survives only near low-pressure conditions. These results show that hcp-ground-state metals do not follow a single structural response under electronic excitation; instead, they span the full range from close-packed competition to pressure-driven bcc stabilization.

The atomic volume associated with each stable phase, shown separately in Fig. 3 and tabulated at the pressure extremes in Table I, clarifies why pressure favors bcc in some of these metals but not others. Although the bcc lattice has a lower geometric packing fraction than the close-packed hcp

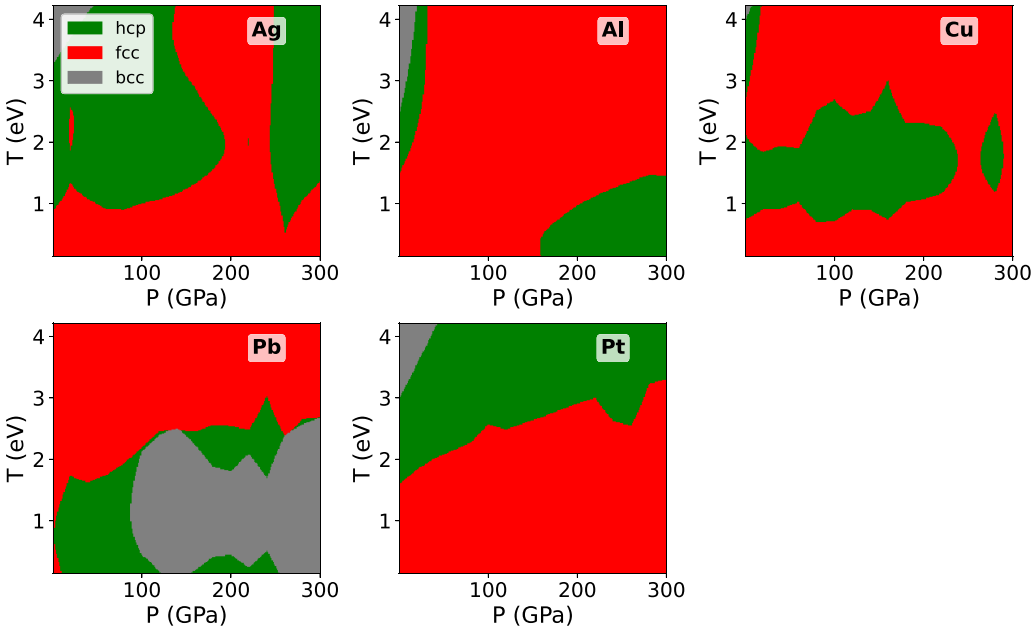


FIG. 2. Gibbs free-energy phase diagrams of fcc-ground-state transition metals (Al, Ag, Cu, Pb, and Pt) as a function of pressure and electronic temperature. The stable phase at each (P, T) point is determined from the minimum Gibbs free energy among hcp, fcc, and bcc structures. The equilibrium atomic volume of the stable phase at each point is shown separately in Fig. 5, with representative values at the pressure extremes collected in Table II. The diagrams reveal distinct classes of behavior within the fcc group. Al remains robustly fcc across nearly the entire phase space, with only a very limited hcp region at high pressure. Ag, Cu, and Pt exhibit pronounced competition within the close-packed manifold, with pressure promoting the hcp phase over wide regions and, in the case of Cu, a broad intermediate-temperature hcp regime. In contrast, Pb shows a qualitatively different response, with a large bcc stability region emerging at elevated pressures, indicating strong volume-driven stabilization.

and fcc lattices, its DFT equilibrium volume is not necessarily larger. In Ti and Zr, where the Gibbs phase diagrams show clear pressure-driven bcc stabilization, bcc has the smallest atomic volume of the three phases at every pressure investigated, so external pressure—which always favors the most compact structure—naturally selects bcc over its close-packed competitors. The same ordering holds for Mg below ∼170 GPa; above this pressure, the ranking inverts and fcc becomes the more compact phase, consistent with the renewed encroachment of fcc stability at the highest pressures visible in Fig. 1. In Cd and Zn, in contrast, bcc never has the smallest volume at any pressure on the grid—fcc and hcp remain more compact throughout—which is consistent with bcc playing essentially no role in their phase diagrams despite compression being applied over the same 0–300 GPa range. Pressure therefore does not intrinsically favor bcc as a lattice type; it favors whichever phase is most compact at the DFT level for that particular element, and this element-specific ordering, rather than a general packing-fraction argument, sets the pressure-driven branch of each phase diagram. All five metals show a comparable overall volume collapse of 48%–65% between 0 and 300 GPa (Table I), while the volume differences between competing phases of the same element are consistently only 1%–3%, an order of magnitude smaller than the total compression—which is why the phase competition is so sensitive to which structure happens to be marginally more compact at a given pressure. Because hcp is the only one of the three candidate lattices whose ideal geometry ($c/a = \sqrt{8/3} \approx 1.633$) is not fixed by symmetry, it is also the only structure capable of departing from close packing without a symmetry-breaking distortion. Figure 4 shows the optimized c/a ratio as a function of pressure for the five hcp-ground-state metals, together with the pressure range over which hcp is actually the thermodynamically stable phase at some elec-

TABLE I. Equilibrium atomic volume of each competing phase at the lowest (∼0 GPa) and highest (∼300 GPa) pressures on the calculated grid, together with the total volume collapse $\Delta V/V_0$ over this range, for the five hcp-ground-state metals of Fig. 1. The pressure dependence of the phase ordering (which structure is most compact at a given P) is discussed in the text.

Element	Phase	V_0 (Å^3/atom)	V_{300} (Å^3/atom)	$\Delta V/V_0$ (%)
Cd	hcp	20.85	10.36	−50.3
	fcc	20.94	10.37	−50.5
	bcc	21.27	10.39	−51.1
Mg	hcp	22.43	7.80	−65.2
	fcc	22.37	7.75	−65.4
	bcc	22.14	7.78	−64.9
Ti	hcp	16.77	7.61	−54.6
	fcc	16.69	7.60	−54.5
	bcc	16.55	7.42	−55.2
Zn	hcp	14.08	7.34	−47.8
	fcc	14.03	7.35	−47.6
	bcc	14.28	7.36	−48.4
Zr	hcp	22.42	10.06	−55.1
	fcc	22.17	10.06	−54.6
	bcc	21.80	9.89	−54.7

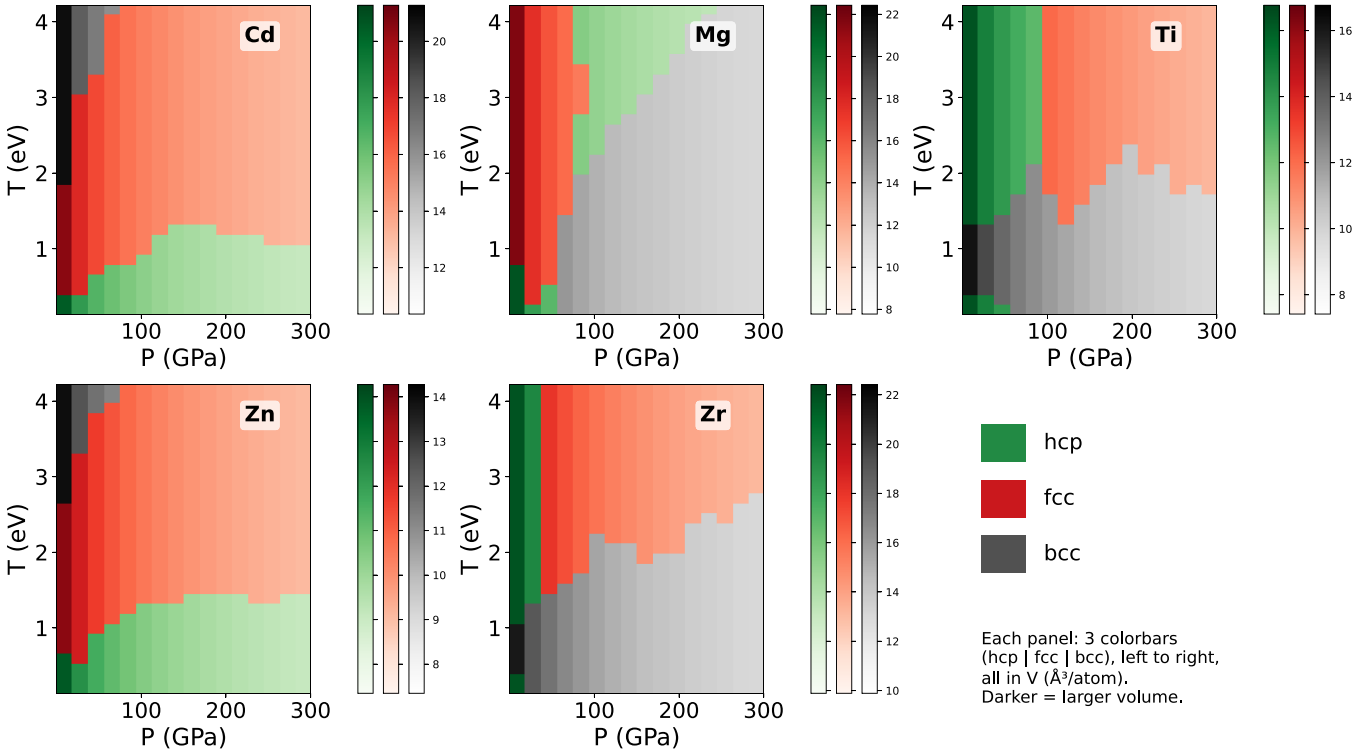


FIG. 3. Equilibrium atomic volume V (Å^3/atom) of the Gibbs-stable phase at each (P, T) point, for the five hcp-ground-state metals of Fig. 1, shown on the raw 16×31 calculation grid (no interpolation). Color hue identifies the stable phase (green = hcp, red = fcc, gray = bcc, matching Fig. 1); within each hue, brightness encodes V on a per-element scale shared across all three phases (darker = larger volume), so that both the identity of the stable phase and its atomic volume are visible simultaneously.

tronic temperature (solid) versus metastable only (dotted). Cd and Zn are markedly anomalous at low pressure ($c/a = 1.91$ and 1.79, respectively, 17% and 9% above ideal), in good agreement with their known experimental room-pressure values (1.89 and 1.86); this anomaly relaxes smoothly toward the ideal ratio by ∼150–200 GPa, entirely within the pressure range over which hcp remains thermodynamically stable for these two elements. Mg, in contrast, stays within 1% of the ideal ratio across its entire stability range, consistent with its more free-electron-like bonding. Ti and Zr show the opposite behavior to Cd and Zn: c/a is close to ideal at low pressure and rises sharply above it at higher pressure, reaching 1.93 and 1.81, respectively—but this rise occurs almost entirely outside the pressure range in which hcp is actually stable (hcp gives way to bcc above 80 GPa in Ti and above 20 GPa in Zr), so the large c/a distortion in these two elements is a property of the metastable lattice rather than one realized in the predicted phase diagram. The anomalous-c/a physics highlighted here is therefore specific to Cd and Zn among the metals studied.

The free-energy phase diagrams of the fcc-ground-state metals exhibit a strongly material-dependent behavior. While Al remains a robust fcc system across nearly the entire pressure-temperature range, other elements exhibit substantial competition between alternative structures. Ag, Cu, and Pt are dominated by competition within the close-packed manifold, with pressure promoting the hcp phase over wide regions of the phase diagram, leading to pronounced fcc-hcp coexistence and, in the case of Cu, a broad intermediate-temperature hcp regime. In contrast, Pb displays a qualitatively different behavior, with a large bcc stability region emerging at elevated pressures, indicating a strong influence of volume effects that overcome the preference for close-packed structures. These results demonstrate that phase behavior of fcc-ground-state metals ranges from robust fcc stability to close-packed competition and, in some cases, pressure-driven stabilization of bcc phases.

The equilibrium volumes underlying Fig. 5 and Table II show that compactness alone is not sufficient to predict where bcc becomes stable; it must be weighed against the internal-energy cost of adopting the bcc lattice, exactly as captured by $\Delta G_{\alpha\beta} = \Delta F_{\alpha\beta}(T) + P\Delta V_{\alpha\beta}$ (Sec. III B). In Pb, bcc has the smallest atomic volume of the three phases over nearly the entire pressure range, mirroring the behavior found for Ti and Zr among the hcp-ground-state metals, and pressure correspondingly stabilizes a substantial bcc region. In Ag, Cu, and Pt, bcc is never the most compact phase at any pressure investigated, consistent with its negligible presence in their phase diagrams; in these metals, the close-packed fcc and hcp lattices instead trade places as the most compact structure; the two are nearly degenerate in Cu, reflecting their shared close-packed coordination. Al is the instructive exception: Above ∼50 GPa, bcc is in fact the most compact of the three phases, by a modest 0.5%–1%, yet the phase diagram remains overwhelmingly fcc, with the small residual competition coming from hcp rather than bcc. This shows that the volume term $P\Delta V$ favoring bcc in Al is more than offset by the energetic term ΔF, so compression does not stabilize bcc even though it is the smallest-volume structure—underscoring that pressure-driven bcc stabilization requires both a volume and an energetic advantage, not compactness alone.

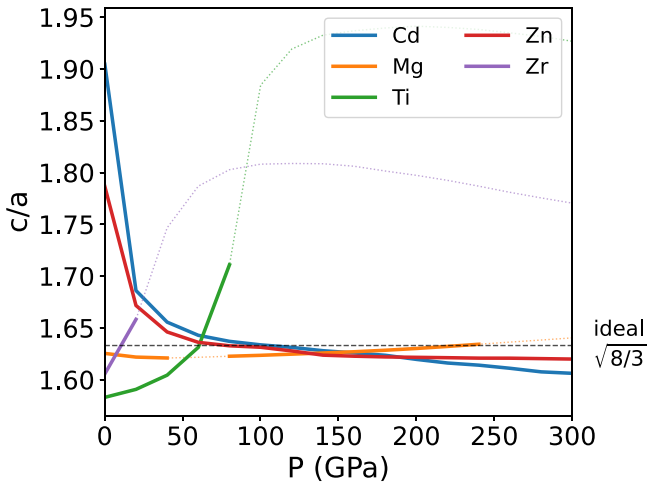


FIG. 4. Optimized hcp c/a ratio as a function of pressure for the five hcp-ground-state metals, relative to the ideal close-packed value $\sqrt{8/3}$ (dashed line). Solid segments mark pressures at which hcp is thermodynamically stable at some electronic temperature in Fig. 1; dotted segments mark pressures at which the optimized hcp structure exists but is metastable (a different phase has lower Gibbs free energy at all temperatures studied).

The phase diagrams of the bcc-ground-state metals show a dominant low-temperature bcc phase in all cases, consistent with bcc being the DFT ground-state structure for each of these elements. With increasing electronic temperature, all five metals show an expansion of the fcc phase, indicating a temperature-driven crossover toward fcc stability; the extent of this crossover is strongly material dependent, ranging from a fcc fraction of ∼59% of the phase diagram in W down to ∼23% in Mo, which shows the weakest, but not negligible, entropy-driven fcc stabilization among the five. A small hcp region also appears in Nb, W, and Mo. These results show that, within the bcc group, structural stability is governed by a competition between the low-temperature cohesive-energy advantage of bcc and entropy-favored fcc phases, with the strength of this competition varying significantly between materials.

TABLE II. Equilibrium atomic volume of each competing phase at the lowest (∼0 GPa) and highest (∼300 GPa) pressures on the calculated grid, together with the total volume collapse $\Delta V/V_0$ over this range, for the five fcc-ground-state metals of Fig. 2. The pressure dependence of the phase ordering (which structure is most compact at a given P) is discussed in the text.

Element	Phase	V_0 (Å^3/atom)	V_{300} (Å^3/atom)	$\Delta V/V_0$ (%)
Al	hcp	16.31	7.56	−53.6
	fcc	16.17	7.62	−52.9
	bcc	16.57	7.51	−54.7
Ag	hcp	16.78	9.71	−42.1
	fcc	16.70	9.71	−41.9
	bcc	16.85	9.72	−42.3
Cu	hcp	11.35	6.81	−40.0
	fcc	11.29	6.80	−39.8
	bcc	11.37	6.82	−40.1
Pb	hcp	29.87	13.18	−55.9
	fcc	29.82	13.22	−55.6
	bcc	29.85	13.17	−55.9
Pt	hcp	15.19	10.35	−31.9
	fcc	15.10	10.33	−31.6
	bcc	15.28	10.35	−32.2

The equilibrium volumes underlying Fig. 7 and Table III show that, in this group, bcc's low-temperature dominance is primarily an energetic rather than a volume effect: Because these are bcc-ground-state elements, bcc already carries a substantial cohesive-energy advantage at $T \to 0$, and this is normally large enough to win even where bcc is not the most compact phase. V is the only element of the five where bcc has the smallest atomic volume at every pressure studied; in Mo, in contrast, bcc has the smallest volume at only 3–16 pressures (hcp is more compact over most of the range), yet bcc still dominates the low-temperature phase diagram because of its energetic advantage. This is the same balance identified for the hcp- and fcc-ground-state metals (Sec. III A), applied in reverse: there, a phase needed both a volume and an energetic advantage to be pressure stabilized; here, bcc's built-in energetic advantage as the ground state is normally sufficient on its own, so the volume ordering plays a comparatively minor role except in determining the detailed shape of the hcp/fcc/bcc boundaries at intermediate temperature.

Figure 8 summarizes the global trends in phase stability extracted from the free-energy calculations. Panel (a) shows that increasing electronic temperature drives a redistribution of stability across all metals as the fraction of bcc phases decreases rapidly, while fcc becomes the dominant structure above $T \sim 0.15$–0.20 Ry, reaching ∼70% of the phase space at the highest temperatures. The hcp fraction remains relatively constant, indicating that it plays a secondary but persistent role. This behavior reflects a systematic weakening of the pressure-stabilized bcc phase under strong electronic excitation and a concurrent stabilization of close-packed structures, particularly fcc. Panel (b) provides a complementary, physically intuitive view by tracking the dominant phase at low pressure for each metal. At low temperatures, the expected ground-state structures are recovered, confirming the consistency of the approach. As temperature increases, many systems undergo transitions toward fcc or, in some cases, hcp, while bcc stability is progressively restricted to a smaller subset of materials. Together, these panels demonstrate that strong electronic excitation reduces structural diversity and drives a convergence toward a simplified structural landscape dominated by close-packed phases, with fcc emerging as the most prevalent high-temperature structure, while the detailed pathway remains strongly material dependent.

The origin of this trend can be examined directly, since the finite-temperature free energy $F(V,T)$ obtained self-consistently at each grid point already encodes the electronic entropy of each phase; differentiating numerically, $S(T) = -\partial F/\partial T$, gives the electronic entropy of hcp, fcc, and bcc. Within the bcc-ground-state group, this comparison is unambiguous: All five metals (Cr, Mo, Nb, V, and W) show $S_{\rm fcc}(T) > S_{\rm bcc}(T)$ at every temperature studied [Fig. 9(a)], which is why all five exhibit a temperature-driven crossover

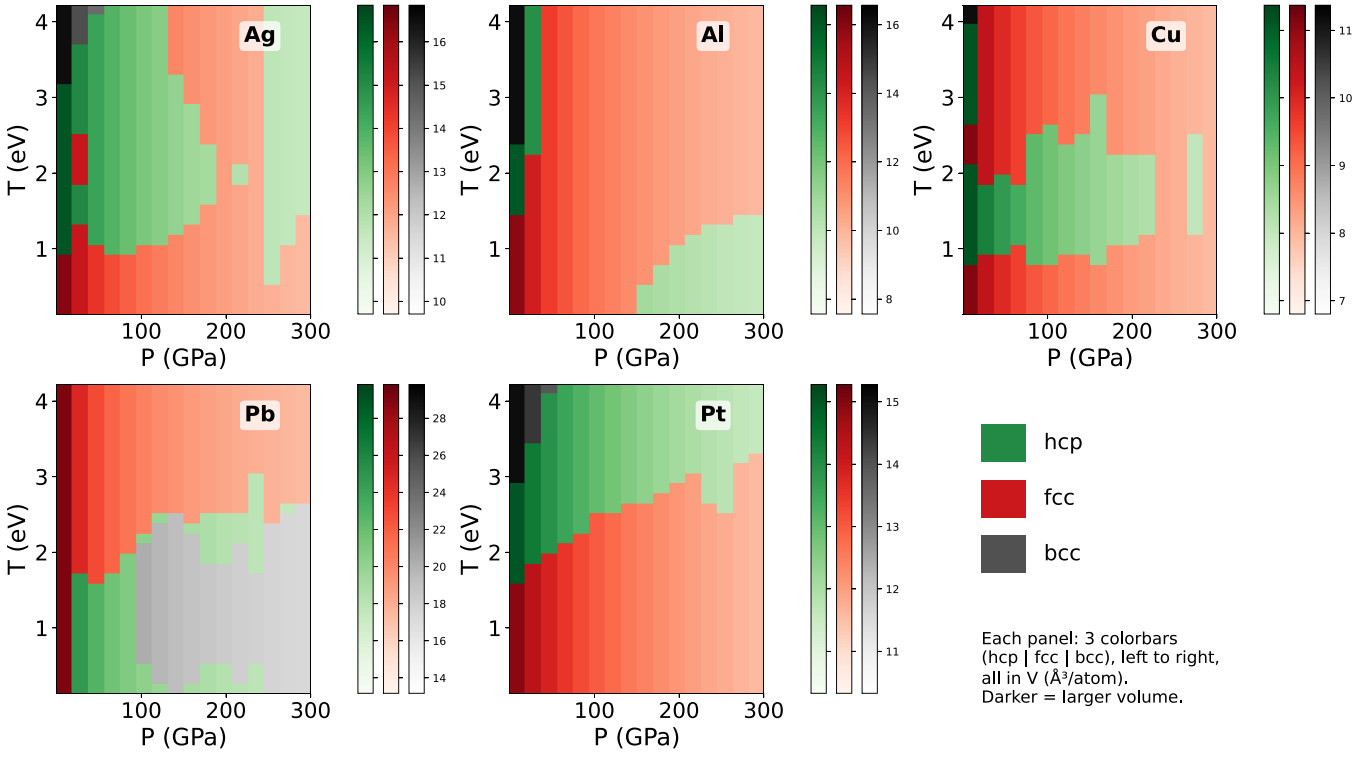


FIG. 5. Equilibrium atomic volume V (Å^3/atom) of the Gibbs-stable phase at each (P, T) point, for the five fcc-ground-state metals of Fig. 2, shown on the raw 16×31 calculation grid. Color convention as in Fig. 3: Hue identifies the stable phase, and brightness encodes V on a per-element scale (darker = larger volume).

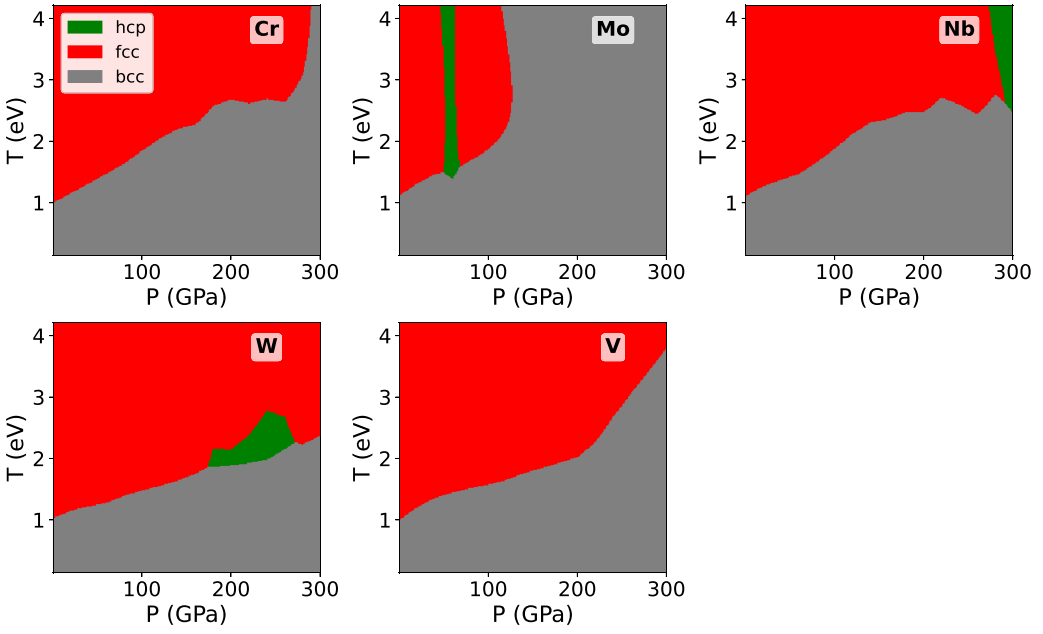


FIG. 6. Gibbs free-energy phase diagrams of bcc-ground-state transition metals (Cr, Mo, Nb, W, and V) as a function of pressure and electronic temperature. The stable phase at each (P, T) point is determined from the minimum Gibbs free energy among hcp, fcc, and bcc structures. The equilibrium atomic volume of the stable phase at each point is shown separately in Fig. 7, with representative values at the pressure extremes collected in Table III. All systems exhibit a dominant bcc phase at low temperatures, reflecting the large cohesive-energy advantage of the ground-state bcc lattice at low pressure. With increasing electronic temperature, all five metals show an expansion of the fcc phase, indicating a temperature-driven crossover toward fcc stability, though the extent of this crossover varies substantially: The fcc fraction of the phase diagram ranges from ∼59% in W down to ∼23% in Mo, which shows the weakest entropy-driven fcc stabilization of the group but is not fcc-free. A small hcp region also appears in Nb, W, and Mo.

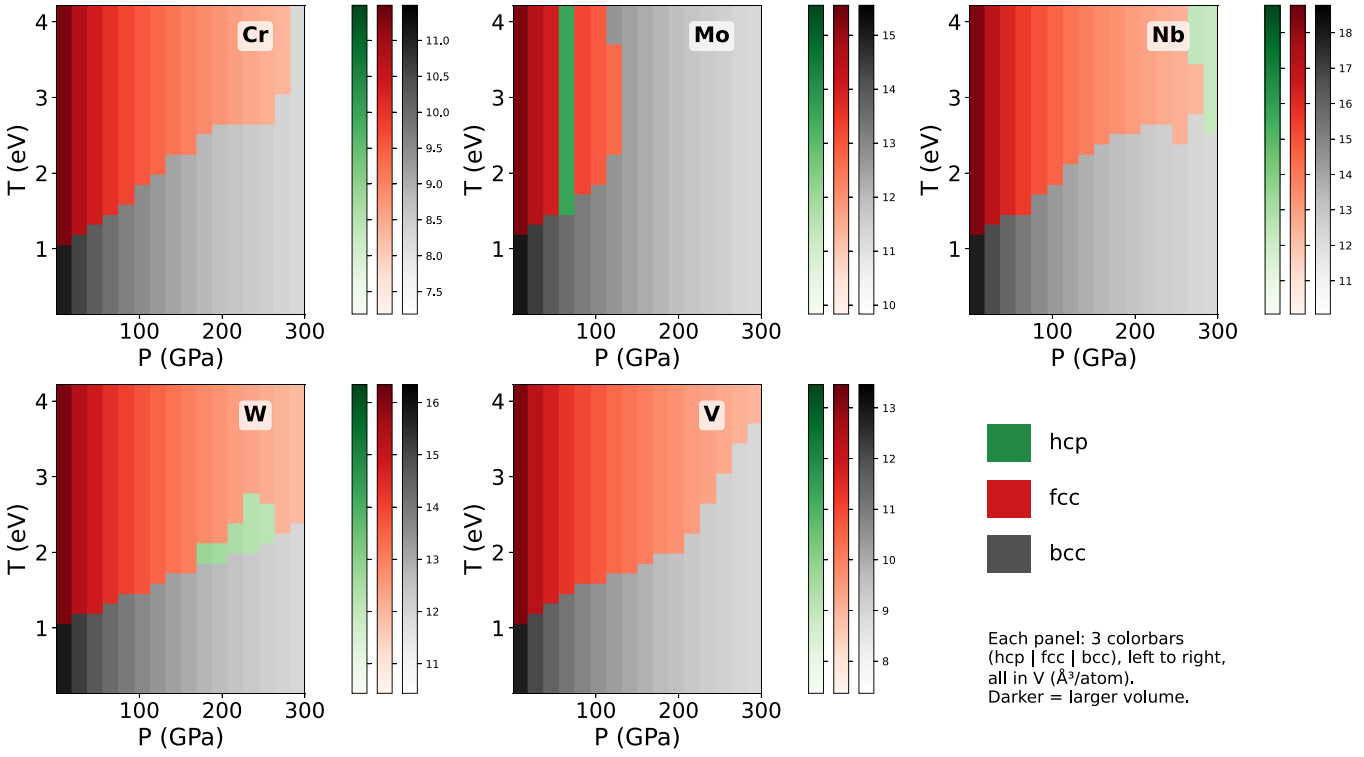


FIG. 7. Equilibrium atomic volume V (Å^3/atom) of the Gibbs-stable phase at each (P, T) point, for the five bcc-ground-state metals of Fig. 6, shown on the raw 16×31 calculation grid. Color convention as in Fig. 3: Hue identifies the stable phase, and brightness encodes V on a per-element scale (darker = larger volume).

from bcc to fcc despite bcc being the $T \to 0$ ground state in every case. The magnitude of this entropy advantage is smallest for Mo across most of the temperature range, consistent with Mo showing the weakest fcc stabilization (∼23% of its phase diagram) of the five bcc-ground-state metals. This trend is not perfectly monotonic across the remaining four metals, however [Fig. 9(b)]: Nb has the largest time-averaged entropy gap but only a middling fcc fraction, while W has a smaller gap yet the largest fcc fraction of the group. This indicates that the $T = 0$ energy difference between phases—not entropy alone—also plays a role in setting the precise fcc fraction, even though the sign of the entropy gap correctly determines whether a bcc-to-fcc crossover occurs at all. More broadly, across all 15 elements, the phase with the largest computed entropy correctly identifies the Gibbs-stable phase at the highest temperature studied (low pressure) in 12 of 15 cases; the three exceptions (Cr, Mo, and W) are cases where hcp has the largest raw entropy of the three candidates yet fcc still wins the free-energy competition, showing that entropy differences alone are necessary but not sufficient to determine the outcome—the $T = 0$ energetic ordering still matters.

B. Helmholtz free-energy phase diagram

To investigate the thermodynamic origin of the phase behavior, we compare phase diagrams constructed from the Helmholtz and Gibbs free energies. The Helmholtz formulation, isolates the contribution of electronic entropy through the $-T\Delta S$ term, allowing us to assess how increasing electronic temperature modifies relative phase stability in the absence of volume relaxation. In contrast, the Gibbs formulation incorporates the additional $P\Delta V$ contribution associated with externally applied pressure, enabling structural selection through differences in atomic volume between competing phases. The comparison between these two descriptions therefore provides a direct means of disentangling the competition between entropy-driven stabilization and pressure-induced volume effects in determining phase stability. It should be emphasized that only Gibbs free-energy phase diagrams correspond to constant-pressure conditions and are therefore appropriate for direct comparison with experimental phase boundaries.

We performed the same analysis for all 15 elements using the Helmholtz free energy F in addition to the Gibbs free energy G. The relationship between the two thermodynamic potentials is given by $G(P, T) = F(V, T) + PV$, where V is the volume per atom. Consequently, the difference in stability between two competing phases α and β can be written as $\Delta G_{\alpha\beta}(P, T) = \Delta F_{\alpha\beta}(T) + P\,\Delta V_{\alpha\beta}$, with $\Delta F_{\alpha\beta} = F_\alpha - F_\beta$ and $\Delta V_{\alpha\beta} = V_\alpha - V_\beta$. The Helmholtz free-energy difference $\Delta F_{\alpha\beta}$ contains both internal energy and entropy contributions, $\Delta F_{\alpha\beta}(T) = \Delta E_{\alpha\beta} - T\,\Delta S_{\alpha\beta}$, so that phase stability is determined by the competition between the entropy term $-T\Delta S$ and the pressure-volume term $P\Delta V$.

For the hcp-ground-state metals (Cd, Mg, Ti, Zn, and Zr), the calculated Helmholtz phase diagrams (Fig. 10) reveal that the stability of the hcp phase is largely confined to low

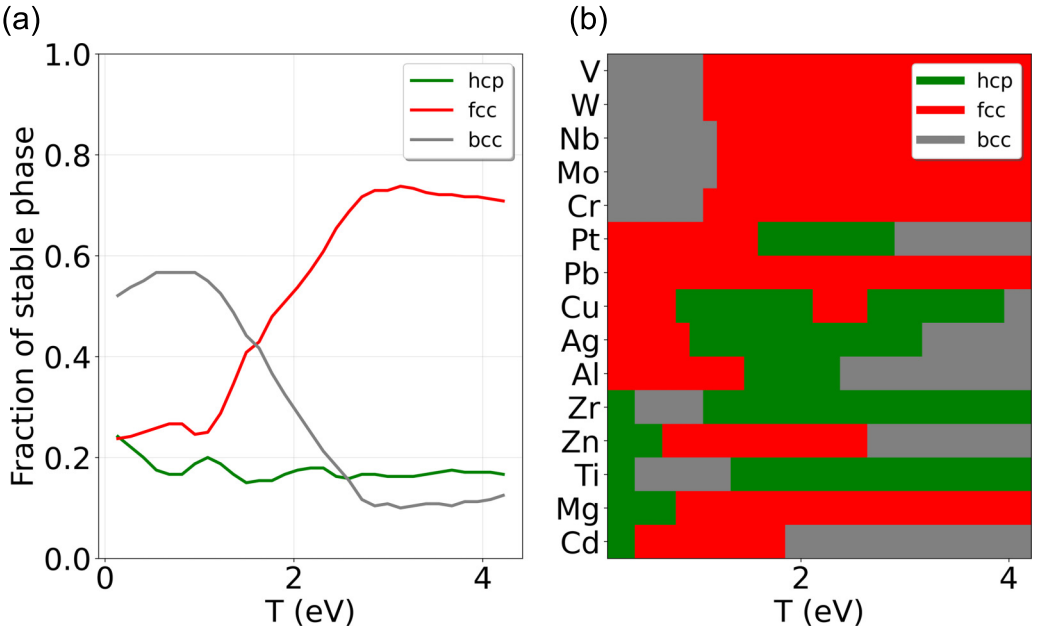


FIG. 8. (a) Fraction of stable crystal structures across all 15 metals as a function of electronic temperature, obtained from Gibbs free-energy phase diagrams. At each (P, T) point, the thermodynamically stable phase is identified from the minimum Gibbs free energy among hcp, fcc, and bcc structures, and the fraction is computed over all pressures and elements. Increasing electronic temperature leads to a systematic suppression of bcc stability and a corresponding increase in fcc dominance, while hcp remains a secondary but persistent phase. (b) Dominant crystal structure as a function of electronic temperature for each metal, evaluated at the lowest pressure point of the phase diagram. This representation reflects the temperature-driven structural evolution under near-ambient pressure conditions. Most metals exhibit a transition from their ground-state structure toward either fcc or hcp at elevated temperatures, with fcc emerging as the most prevalent high-temperature phase, while bcc remains stable primarily at low temperatures or in selected materials.

electronic temperatures and limited pressure ranges. With increasing temperature, most systems exhibit a progressive reduction of the hcp stability field, accompanied by the emergence and eventual dominance of the fcc phase. This trend is particularly pronounced in Ti, Zr, Zn, and Cd, where fcc becomes the energetically preferred structure over a broad region of the phase diagram at elevated temperatures. The primary exception is Mg, which retains a relatively large hcp stability region across the explored pressure range, reflecting its weaker d-electron character and more free-electron-like bonding.

For the fcc-ground-state metals (Al, Ag, Cu, Pb, and Pt), the phase diagrams (Fig. 11) show that the fcc structure remains robust across a wide range of pressures and temperatures, with only limited competition from hcp or bcc phases. In particular, Al and Pb exhibit an almost complete dominance

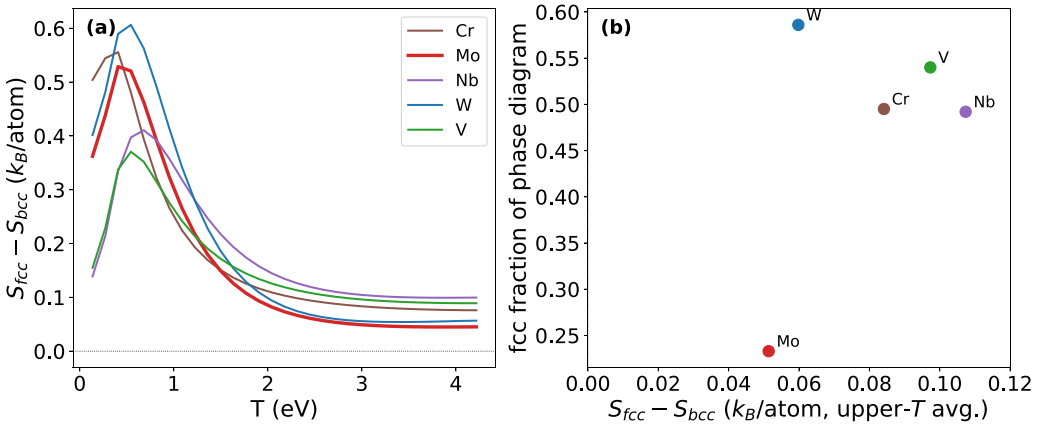


FIG. 9. Electronic entropy analysis for the bcc-ground-state metals, obtained by numerical differentiation of the finite-temperature free energy, $S(T) = -\partial F/\partial T$, at the lowest pressure studied. (a) $S_{\rm fcc} - S_{\rm bcc}$ as a function of temperature for all five bcc-ground-state metals: The gap is positive throughout for every element, explaining why all five show a bcc-to-fcc crossover, with Mo (bold) showing the smallest gap at high temperature. (b) The time-averaged (upper-temperature) entropy gap plotted against the fraction of each element's Gibbs phase diagram occupied by fcc: Mo is the clear outlier at low values of both quantities, though the ranking of the remaining four elements is not strictly monotonic, indicating that $T = 0$ energetics also contribute to the final balance.

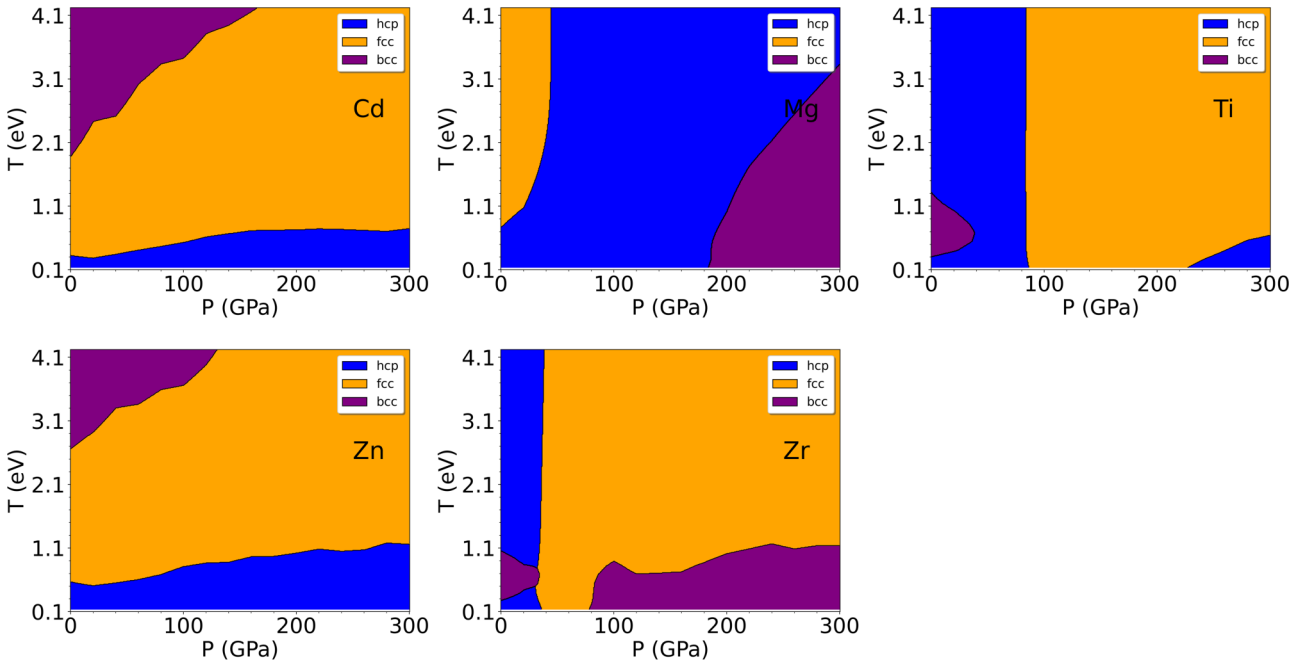


FIG. 10. Helmholtz phase diagrams of hcp-ground-state metals Cd, Mg, Ti, Zn, and Zr.

of the fcc phase throughout the explored thermodynamic space, indicating that strong electronic excitation does not significantly alter their structural preference. In contrast, Ag, Cu, and Pt display a more pronounced competition between fcc and hcp structures, especially at elevated temperatures and intermediate pressures. Nevertheless, this competition remains confined to the close-packed family, and no substantial stabilization of bcc phases is observed.

For the bcc-ground-state metals (Cr, Mo, W, V, and Nb), the phase diagrams, shown in Fig. 12, exhibit a markedly different low-temperature behavior but converge toward a similar high-temperature regime. At low electronic temperatures, the bcc phase is dominant across a wide pressure range, consistent with the known ground-state structures of these elements. However, with increasing temperature, the stability of the bcc phase is progressively reduced, and regions of fcc and, in some cases, hcp stability emerge and expand. This effect is particularly evident in V and Nb, where close-packed phases occupy a significant portion of the phase diagram at elevated temperatures. Even in refractory systems such as Mo and W,

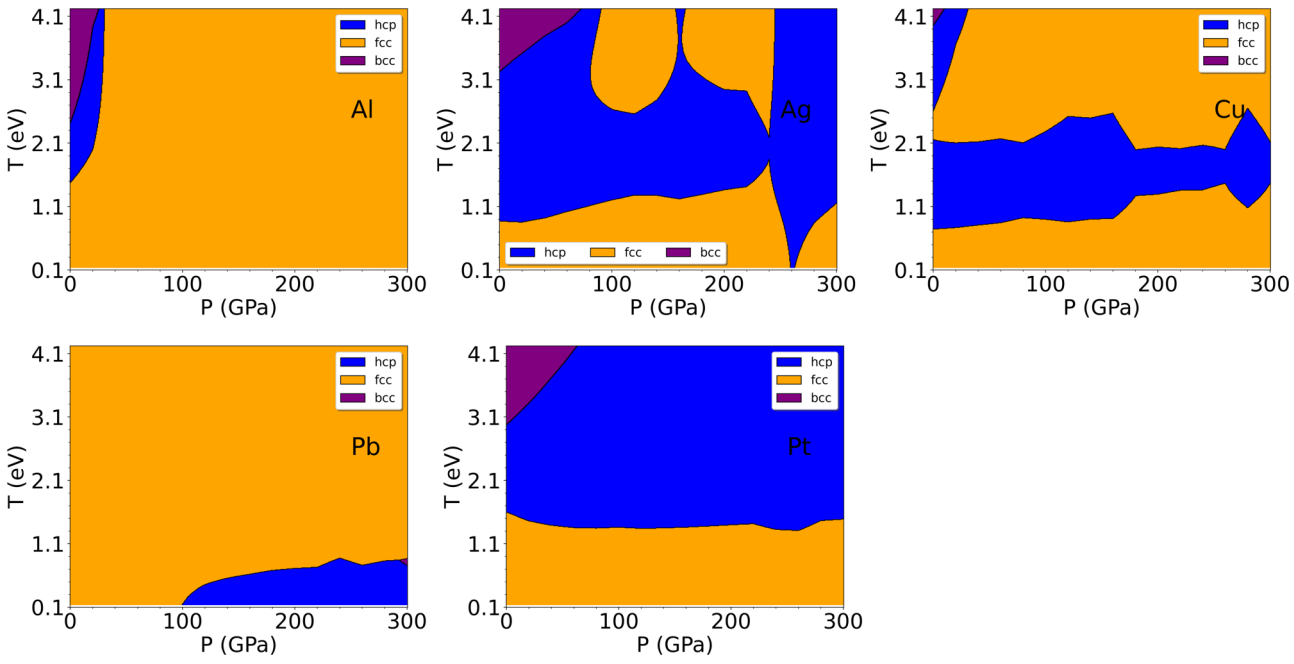


FIG. 11. Helmholtz phase diagrams of fcc-ground-state metals Al, Ag, Cu, Pb, and Pt.

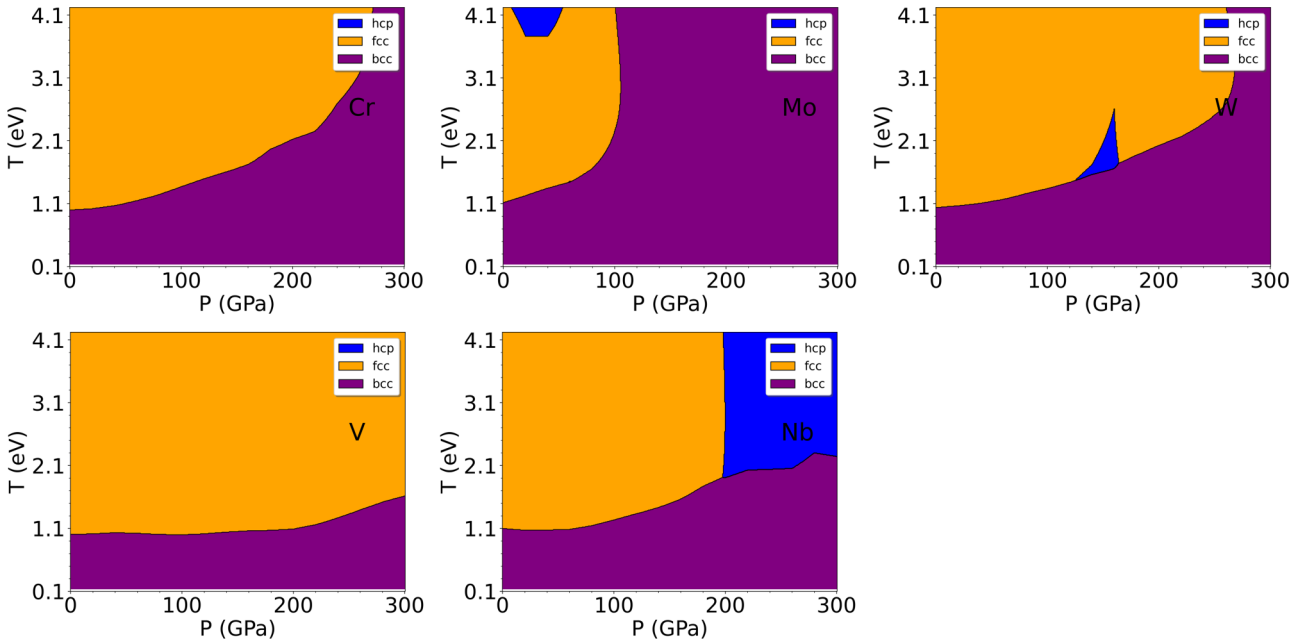


FIG. 12. Pressure-temperature Helmholtz phase diagrams of bcc-ground-state metals Cr, Mo, W, V, and Nb.

where bcc remains comparatively robust, the phase space is no longer exclusively bcc dominated.

IV. CONCLUSION AND OUTLOOK

We have investigated electronically driven solid-solid phase transitions in transition metals using finite-temperature density functional theory, constructing Gibbs free-energy phase diagrams for 15 elements over a wide pressure-temperature range. The results provide a comprehensive picture of how structural stability evolves under electronic excitation, revealing a progressive reduction in the number of competing phases as temperature increases. This evolution is accompanied by a redistribution of stability toward simpler crystal structures, most notably fcc, while bcc stability becomes increasingly restricted to higher-pressure conditions and hcp persists as a secondary phase in selected systems.

TABLE III. Equilibrium atomic volume of each competing phase at the lowest (∼0 GPa) and highest (∼300 GPa) pressures on the calculated grid, together with the total volume collapse $\Delta V/V_0$ over this range, for the five bcc-ground-state metals of Fig. 6.

Element	Phase	V_0 (Å^3/atom)	V_{300} (Å^3/atom)	$\Delta V/V_0$ (%)
Cr	hcp	11.51	7.15	−37.9
	fcc	11.49	7.17	−37.6
	bcc	11.18	7.19	−35.7
Mo	hcp	15.62	9.70	−37.9
	fcc	15.55	9.70	−37.7
	bcc	15.32	9.83	−35.8
Nb	hcp	18.66	10.08	−46.0
	fcc	18.77	10.03	−46.6
	bcc	18.09	10.06	−44.4
W	hcp	16.43	10.40	−36.7
	fcc	16.34	10.43	−36.2
	bcc	16.03	10.48	−34.7
V	hcp	13.38	7.50	−44.0
	fcc	13.46	7.50	−44.3
	bcc	13.00	7.37	−43.4

The detailed phase behavior depends strongly on the ground-state structure and atomic volume. Bcc-ground-state metals generally retain bcc stability at low temperatures and pressures, with fcc emerging at elevated temperatures in all five cases, though to a degree that varies substantially between elements (Sec. III A). Fcc-ground-state metals display a broader range of responses, including robust fcc stability, competition within the close-packed manifold, and, in some cases, pressure-driven stabilization of bcc. Hcp-ground-state metals exhibit the widest diversity, spanning regimes of hcp-fcc competition, strong bcc stabilization, and three-phase coexistence. These results show that structural stability under electronic excitation is determined by the balance between electronic effects and compression, which together select among a reduced set of crystal structures and define a material-dependent phase landscape.

A detailed comparison between phase diagrams constructed from the Helmholtz free energy F and the Gibbs free energy G provides insight into the relative importance of the entropy term $-T\Delta S$ and the pressure-volume contribution $P\Delta V$ in determining phase stability. In the high-temperature, low-pressure regime, both approaches yield consistent phase boundaries, indicating that stability is primarily governed by entropy-driven effects. In contrast, significant deviations emerge at elevated pressures, where the inclusion of the $P\Delta V$ term alters the relative stability of competing phases, most notably stabilizing bcc structures with smaller atomic volumes. These comparisons show that the trends observed in the Gibbs phase diagrams arise from a balance between entropy-driven stabilization at high temperature and compression-driven

effects at high pressure, with the dominant contribution varying across the pressure-temperature space.

More broadly, this work introduces electronic entropy as an additional thermodynamic dimension in phase stability and equations of state. Under strong electronic excitation, entropy can modify structural stability independently of density, shifting phase boundaries relative to conventional compression pathways. Such effects may contribute to discrepancies between static and dynamic compression experiments [14,15]. Capturing this physics in predictive simulations will require the development of interatomic potentials that explicitly incorporate electronic excitation and entropy. At the same time, emerging ultrafast pump-probe techniques, combining femtosecond optical or x-ray excitation with time-resolved diffraction and spectroscopy, provide a promising route to experimentally probe these entropy-driven structural transformations and to test the universal behavior identified here. Direct experimental support for pressure-driven bcc stabilization—the mechanism identified in Sec. III A for Ti, Zr, and Pb—has recently emerged from dynamic x-ray diffraction measurements on iron compressed above 200 GPa and probed near its melting curve with the European XFEL, where a bcc phase is observed to form under these conditions [44]. That measurement probes lattice rather than electronic temperature, so it is not a direct test of the electronic-entropy mechanism explored here, but it demonstrates experimentally that bcc stabilization under compression is physically realized in a transition metal, reinforcing the plausibility of the volume- and energy-based picture developed above.

ACKNOWLEDGMENTS

We acknowledge the support of the Leverhulme Trust under Grant Agreement No. RPG-2023-253. S.A. and T.D.K. acknowledge the computing time provided to them on the high-performance computers at the NHR Center in Paderborn (PC2).

DATA AVAILABILITY

There are no publicly available research data or software supporting this manuscript. Requests for further information or data should be sent to the authors.

[1] I. B. Bersuker, *Electronic Structure and Properties of Transition Metal Compounds: Introduction to the Theory* (Wiley–Blackwell, Hoboken, New Jersey, 1996).

[2] A. B. Belonoshko, R. Ahuja, and B. Johansson, Quasi–*ab initio* molecular dynamic study of Fe melting, Phys. Rev. Lett. **84**, 3638 (2000).

[3] G. Steinle-Neumann, L. Stixrude, R. Cohen, and O. Gülseren, Elasticity of iron at the temperature of the Earth's inner core, Nature (London) **413**, 57 (2001).

[4] L. Dubrovinsky, N. Dubrovinskaia, O. Narygina, I. Kantor, A. Kuznetzov, V. B. Prakapenka, L. Vitos, B. Johansson, A. S. Mikhaylushkin, S. I. Simak, and I. A. Abrikosov, Body-centered cubic iron-nickel alloy in Earth's core, Science **316**, 1880 (2007).

[5] L. Vočadlo, D. Alfè, M. J. Gillan, I. G. Wood, J. P. Brodholt, and G. David Price, Possible thermal and chemical stabilization of body-centred-cubic iron in the Earth's core, Nature (London) **424**, 536 (2003).

[6] E. Beaurepaire, J. C. Merle, A. Daunois, and J. Y. Bigot, Ultrafast spin dynamics in ferromagnetic nickel, Phys. Rev. Lett. **76**, 4250 (1996).

[7] V. Recoules, J. Clérouin, G. Zérah, P. M. Anglade, and S. Mazevet, Effect of intense laser irradiation on the lattice stability of semiconductors and metals, Phys. Rev. Lett. **96**, 055503 (2006).

[8] R. Ernstorfer, M. Harb, C. T. Hebeisen, G. Sciaini, T. Dartigalongue, and R. J. Dwayne Miller, The formation of warm dense matter: Experimental evidence for electronic bond hardening in gold, Science **323**, 1033 (2009).

[9] O. S. Humphries, R. S. Marjoribanks, Q. Y. van den Berg, E. C. Galtier, M. F. Kasim, H. J. Lee, A. J. F. Miscampbell, B. Nagler, R. Royle, J. S. Wark, and S. M. Vinko, Probing the electronic structure of warm dense nickel via resonant inelastic X-ray scattering, Phys. Rev. Lett. **125**, 195001 (2020).

[10] G. Kang, G. Lee, S. Azadi, R. Carley, L. L. Guyader, L. P. Hoang, H. B. Kim, M. Kim, C. Lee, L. Mercadier, G. Mercurio, S. Parchenko, A. Seong, D. Shin, M. Teichmann, B. E. Van Kuiken, Z. Yin, S. M. Vinko, A. Scherz, and B. I. Cho, Nonequilibrium electron-phonon and electron-ion couplings in warm dense copper, Appl. Surf. Sci. **713**, 164304 (2025).

[11] S. Sundaram and E. Mazur, Inducing and probing non-thermal transitions in semiconductors using femtosecond laser pulses, Nat. Mater. **1**, 217 (2002).

[12] J. Oitmaa and R. R. P. Singh, Phase diagram of the frustrated quantum-*XY* model on the honeycomb lattice studied by series expansions: Evidence for proximity to a bicritical point, Phys. Rev. B **89**, 104423 (2014).

[13] M. Harb, R. Ernstorfer, C. T. Hebeisen, G. Sciaini, W. Peng, T. Dartigalongue, M. A. Eriksson, M. G. Lagally, S. G. Kruglik, and R. J. D. Miller, Electronically driven structure changes of Si captured by femtosecond electron diffraction, Phys. Rev. Lett. **100**, 155504 (2008).

[14] C. Crépisson, A. Amouretti, M. Harmand, C. Sanloup, P. Heighway, S. Azadi, D. McGonegle, T. Campbell, J. Pintor, D. A. Chin, *et al.*, Shock-driven amorphization and melting in Fe_2O_3, Phys. Rev. B **111**, 024209 (2025).

[15] A. Amouretti, C. Crépisson, S. Azadi, F. Brisset, D. Cabaret, T. Campbell, D. A. Chin, G.W. Collins, L. Hansen, G. Fiquet, *et al.*, Isostructural phase transition of Fe_2O_3 under laser shock compression, Phys. Rev. Lett. **134**, 176102 (2025).

[16] J.-W. Lee, M. Kim, G. Kang, S. M. Vinko, L. Bae, M. S. Cho, H.-K. Chung, M. Kim, S. Kwon, G. Lee, C. H. Nam, S. H. Park, J. H. Sohn, S. H. Yang, U. Zastrau, and B. I. Cho, Investigation of nonequilibrium electronic dynamics of warm dense copper with femtosecond X-ray absorption spectroscopy, Phys. Rev. Lett. **127**, 175003 (2021).

[17] A. S. Johnson, D. Perez-Salinas, K. M. Siddiqui, S. C. S. Kim, K. Volckaert, P. E. Majchrzak, S. Ulstrup, N. Agarwal,

K. Hallman, R. F. Haglund, Jr., *et al.*, Ultrafast X-ray imaging of the light-induced phase transition in VO_2, Nat. Phys. **19**, 215 (2022).

[18] S. Wall, S. Yang, L. Vidas, M. Chollet, M. Glownia, M. Kozina, T. Katayama, T. Henighan, M. Jiang, T. A. Miller, D. A. Reis, L. A. Boatner, O. Delaire, and M. Trigo, Ultrafast disordering of vanadium dimers in photoexcited VO_2, Science **362**, 572 (2018).

[19] K. Sokolowski-Tinten, C. Blome, J. Blums, A. Cavalleri, C. Dietrich, A. Tarasevitch, I. Uschmann, E. Förster, M. Kammler, M. Horn-von-Hoegen, and D. von der Linde, Femtosecond X-ray measurement of coherent lattice vibrations near the Lindemann stability limit, Nature (London) **422**, 287 (2003).

[20] M. Z. Mo, Z. Chen, R. K. Li, M. Dunning, B. B. L. Witte, J. K. Baldwin, L. B. Fletcher, J. B. Kim, A. Ng, R. Redmer, A. H. Reid, P. Shekhar, X. Z. Shen, M. Shen, K. Sokolowski-Tinten, Y. Y. Tsui, Y. Q. Wang, Q. Zheng, X. J. Wang, and S. H. Glenzer, Heterogeneous to homogeneous melting transition visualized with ultrafast electron diffraction, Science **360**, 1451 (2018).

[21] J. G. Fujimoto, J. M. Liu, E. P. Ippen, and N. Bloembergen, Femtosecond laser interaction with metallic tungsten and nonequilibrium electron and lattice temperatures, Phys. Rev. Lett. **53**, 1837 (1984).

[22] S. Azadi, J. S. Wark, and S. M. Vinko, Nonthermal solid-solid phase transition in ferromagnetic iron, Phys. Rev. B **110**, 214434 (2024).

[23] S. Azadi, J. S. Wark, and S. M. Vinko, Lattice stability of ultrafast-heated gold, Sci. Rep. **15**, 5350 (2025).

[24] S. Azadi and S. M. Vinko, Electronic temperature driven phase stability and structural evolution of iron at high pressure, Phys. Rev. B **112**, 134103 (2025).

[25] S. Azadi, S. M. Vinko, A. Principi, T. D. Kühne, and M. S. Bahramy, Electronic-entropy-driven solid-solid phase transitions in elemental metals, Phys. Rev. Mater. **10**, 045001 (2026).

[26] S. Azadi, A. Principi, and M. S. Bahramy, Hot electron driven structural expansion and magnetic collapse in bilayer FeSe, Phys. Rev. B **111**, 115118 (2025).

[27] S. Anisimov, B. Kapeliovich, and T. Perelman, Electron emission from metal surfaces exposed to ultrashort laser pulse, Zh. Eksp. Teor. Fiz. **66**, 776 (1974) [Sov. Phys.-JETP **39**, 375 (1974)]

[28] V. Alexopoulou and A. Markopoulos, A critical assessment regarding two-temperature models: An investigation of the different forms of two-temperature models, the various ultrashort pulsed laser models and computational methods, Arch. Comput. Methods Eng. **31**, 93 (2024).

[29] N. D. Mermin, Thermal properties of the inhomogeneous electron gas, Phys. Rev. **137**, A1441 (1965).

[30] A. Pribram-Jones, S. Pittalis, E. Gross, and K. Burke, Thermal density functional theory in context, in *Frontiers and Challenges in Warm Dense Matter*, edited by F. Graziani, M. P. Desjarlais, R. Redmer, S. B. Trickey (Springer Nature, Berlin, Germany, 2014), Vol. 25, p. 60.

[31] S. Pittalis, C. R. Proetto, A. Floris, A. Sanna, C. Bersier, K. Burke, and E. K. U. Gross, Exact conditions in finite-temperature density-functional theory, Phys. Rev. Lett. **107**, 163001 (2011).

[32] J. W. Dufty and S. B. Trickey, Scaling, bounds, and inequalities for the noninteracting density functionals at finite temperature, Phys. Rev. B **84**, 125118 (2011).

[33] K. Burke, J. C. Smith, P. E. Grabowski, and A. Pribram-Jones, Exact conditions on the temperature dependence of density functionals, Phys. Rev. B **93**, 195132 (2016).

[34] N. Ashcroft and N. Mermin, *Solid State Physics* (Saunders College Publishing, Philadelphia, Pennsylvania, 1976).

[35] G. Grimvall, B. Magyari-Köpe, V. Ozoliņš, and K. A. Persson, Lattice instabilities in metallic elements, Rev. Mod. Phys. **84**, 945 (2012).

[36] D. A. Porter and K. E. Easterling, *Phase Transformations in Metals and Alloys*, 2nd ed. (Chapman & Hall, London, 1992).

[37] S. Azadi, N. D. Drummond, and S. M. Vinko, Correlation energy of the paramagnetic electron gas at the thermodynamic limit, Phys. Rev. B **107**, L121105 (2023).

[38] S. Azadi, N. D. Drummond, and S. M. Vinko, Correlation energy of the spin-polarized electron liquid studied using quantum Monte Carlo simulations, Phys. Rev. B **108**, 115134 (2023).

[39] V. V. Karasiev, T. Sjostrom, J. Dufty, and S. B. Trickey, Accurate homogeneous electron gas exchange-correlation free energy for local spin-density calculations, Phys. Rev. Lett. **112**, 076403 (2014).

[40] V. S. Filinov, V. E. Fortov, M. Bonitz, and Z. Moldabekov, Fermionic path-integral Monte Carlo results for the uniform electron gas at finite temperature, Phys. Rev. E **91**, 033108 (2015).

[41] T. Schoof, S. Groth, J. Vorberger, and M. Bonitz, *Ab initio* thermodynamic results for the degenerate electron gas at finite temperature, Phys. Rev. Lett. **115**, 130402 (2015).

[42] P. Giannozzi, S. Baroni, N. Bonini, M. Calandra, R. Car, C. Cavazzoni, D. Ceresoli, G. L. Chiarotti, M. Cococcioni, I. Dabo, *et al.*, QUANTUM ESPRESSO: A modular and open-source software project for quantum simulations of materials, J. Phys.: Condens. Matter **21**, 395502 (2009).

[43] J. P. Perdew, K. Burke, and M. Ernzerhof, Generalized gradient approximation made simple, Phys. Rev. Lett. **77**, 3865 (1996).

[44] Z. Konôpková, E. Edmund, O. B. Ball, A. Dewaele, H. Ginestet, R. J. Husband, N. Jaisle, C. Strohm, M. S. Anae, D. Antonangeli, *et al.*, Observation of body-centered cubic iron above 200 gigapascals, Phys. Rev. B **114**, 094103 (2026).